Research on influencing factors and compensation methods of the azimuth cutoff wavelength based on multiview synthetic aperture radar wave synchronization data

Yong Wan[1], Xiaoyu Zhang[1], Yongshou Dai[1], Ligang Li[1], and Xiaojun Qu[1]

[1]College of Ocean and Space Information, China University of Petroleum, Qingdao, China

Corresponding author: Yong Wan, email: wanyong@upc.edu.cn

Abstract: Due to the nonlinear effect of velocity bunching modulation, azimuth cutoff occurs when waves are propagating along the azimuth direction. This is an inherent disadvantage of synthetic aperture radar (SAR) wave observation and makes it impossible to obtain complete wave information. For a single SAR observation, the problem of the azimuth cutoff wavelength of ocean waves can be solved to some extent by the cooperative observations of SAR satellites. It is necessary to use multiple SAR satellites to achieve simultaneous observation of the same ocean area to obtain multiview SAR ocean wave synchronization data. At present, it is impossible to acquire multiview synchronization data based on in-orbit SARs. Therefore, this paper first carried out imaging simulations of multiview SAR ocean wave synchronization data. Second, the Max Planck Institute (MPI) method was used to obtain the optimum wave spectrum of synchronous data. The influencing factors of the azimuth cutoff wavelength were analyzed by using the measured SAR data. Based on the analysis results, a new method of multiview wave spectrum data fusion is proposed to realize azimuth cutoff compensation. The azimuth cutoff compensation effect is evaluated by using the inversion results of the azimuth cutoff before and after spectral data fusion, the significant wave height and the mean wave period. The results show that the azimuth cutoff compensation method established in this paper can solve the problem of information loss caused by azimuth cutoff to some extent, improve the ability of SAR wave observation, and lay a foundation for SAR wave operational observation.

Keywords: multiview SAR wave synchronization data; wave spectrum data fusion; azimuth cutoff wavelength compensation

1. Introduction

Ocean waves are mostly generated by local winds and are mainly classified into two categories: wind sea and swell [*Ganguly D et al., 2015*]. Studying the formation and evolution mechanism of ocean waves has become an important research field in oceanography. Synthetic aperture radar (SAR) is an effective means of observing large areas of ocean waves, as this technique can provide information on two-dimensional (2D) ocean wave spectra. The spatial resolution of SAR is very high, the observation results are not affected by near-shore terrain, and SAR can detect fine results for a wide range of waves. Alpers [*Alpers and Werner, 1985*] and Hasselmann [*K. Hasselmann et al., 1985*] studied the mechanism of SAR wave imaging in detail, pointing out that tilt modulation, hydrodynamic modulation and velocity bunching modulation are three main modulation mechanisms in the process of SAR wave imaging. However, due to the nonlinear effects of velocity bunching modulation in the azimuth direction, SAR can only detect waves with wavelengths greater than a certain threshold. This threshold is called the azimuth cutoff wavelength, or simply the azimuth cutoff. Due to the effect of the azimuth cutoff, SAR cannot observe complete wave information, which hinders the operational applications of SAR. Studying cutoff wavelength

compensation technology can improve SAR's ability to observe waves and enable SAR to observe more complete wave information.

The factors that affect the azimuth cutoff include significant wave height, wind speed at 10 m height of ocean surface, wave orbital velocity, etc. Vachon P et al. [*1994*] pointed out that the distance-velocity ratio R/V is the key parameter for generating azimuth truncation. A larger R/V indicated that an SAR image spectrum was more sensitive to the azimuth cutoff and imaging nonlinearity. Kerbaol V et al. [*1996*] proposed that the azimuth cutoff was a function of wind speed and significant wave height. Hasselmann et al. [*1991*] analyzed the relationship between the azimuth cutoff wavelength and the modulation transfer function. Based on the image data acquired by ERS-1, Marghany et al. [*2002*] used quasi-linear transformation to estimate the significant wave height of the azimuth cutoff. Ren et al. [*2014*] estimated significant wave height by using the azimuth cutoff of C-band single-polarization SAR images through a look-up table model and an empirical model. Stopa J.E et al. [*2015*] used Envisat Advanced SAR (ASAR) wave model data and buoy data to establish a relationship between the azimuth cutoff and wave orbital velocity. G. Grieco et al. [*2016*] studied the relationship between the azimuth cutoff and wind speed and significant wave height using Sentinel-1 data. Corcione et al. [*2018*] proposed an azimuth cutoff implementation method to retrieve ocean surface wind speed from measured SAR imagery. Based on the quad-polarized Radarsat-2 and Gaofen-3 products, Li V et al. [*2019*] analyzed the dependence of the azimuth cutoff on polarization and incidence angle. Most of the above studies were devoted to mutual estimation of the azimuth cutoff and wave parameters. At present, there is no research on eliminating and compensating for the influence of the azimuth cutoff. Azimuth cutoff compensation is the research work of this paper. The precondition of this work is to acquire multiview SAR wave synchronization data by satellite network cooperative observations. In the literature, Lyzenga and Malinas [*1996*] corrected the azimuth cutoff by measuring a wave spectrum with dual-antenna SAR and put forward the prospect that the azimuth cutoff effect could be compensated by two SAR satellites in the future. That work can be seen as a prototype of azimuth cutoff compensation.

At present, in-orbit satellites cannot realize simultaneous observation in the same ocean area with different observation directions, and it is impossible to obtain multiview synchronization data. Therefore, it is only possible to obtain multiview synchronization data through imaging simulation technology and carry out preresearch work on multiple SAR cooperative observation waves, which lays a foundation for future observation of SAR satellite observation waves. However, most of the current studies performed imaging simulations of a single SAR, and synchronous imaging simulations of multiple SARs have not been studied. Based on a single SAR imaging simulation, imaging simulation of networked satellites with three SARs is carried out, and multiview SAR wave synchronization data are simulated. By means of simulation, there are two methods to obtain ocean surface SAR images. The first method is to directly simulate SAR images of the ocean based on the ocean surface model, the electromagnetic scattering model and the imaging mechanism of SAR for the waves. Although this method avoids calculation of complex raw SAR data, it cannot comprehensively reflect the characteristics of an SAR system. The second method is to indirectly obtain ocean SAR images by simulating the generation of SAR echo signals [*Franceschetti G et al., 1998*]. The imaging method used in this paper is the second method. Compared with the first method, this method has the advantages of being independent of the imaging model and high accuracy of imaging results.

After obtaining wave synchronization data, it is necessary to invert the wave spectrum observed

by SARs. There is a nonlinear transformation relationship between the SAR image spectrum and the wave spectrum. Through study, researchers have proposed a variety of SAR wave spectrum inversion methods. Hasselmann et al. [*1991*] deduced a nonlinear transformation of the SAR image spectrum to the wave direction spectrum. Based on the transformation, the Max Planck Institute (MPI) algorithm was developed. In 1996, Hasselmann et al. [*1996*] improved the MPI algorithm based on the original theory. He [*1999*] proposed a parametric wave spectrum inversion method to realize the application of SAR wave spectrum inversion in the China Sea. Mastenbroek and De Valk [*2000*] proposed an inversion semiparametric method, SPRA, which is based on ERS wave mode data. The initial guess is the wind-wave spectrum estimated from the wind information observed by a scatterometer. Engen and Johnsen [*1995*] proposed a cross-spectrum algorithm that solves the 180 ° mapping ambiguity in the direction of wave propagation while reducing speckle noise. Schulz et al. [2005] proposed an improved nonlinear inversion algorithm, PARSA, which is a combination of the MPI algorithm and a cross-spectrum algorithm. The MPI algorithm was the earliest proposed wave spectrum inversion algorithm. The inversion results are relatively accurate and are the basis of other inversion methods. Therefore, this paper chooses the MPI algorithm to realize wave spectrum inversion of synchronous ocean wave data.

The chapter structure of this paper is as follows: In Section 2, the basic principles of SAR imaging simulation and the MPI algorithm are introduced. In Section 3, estimation of the azimuth cutoff and the data fusion method are described. Section 4 analyzes the results obtained in this paper. Conclusions are provided in the final section.

2. Materials and Methods

2.1 Simulation of multiview SAR wave synchronization data

The simulation of multiview SAR wave synchronization data can comprise wave spectrum and ocean surface simulation, backscattering coefficient calculation, echo signal generation, ocean SAR imaging and synchronous ocean wave data [*Wan Y et al,. 2019*]. There is a progressive relationship among the steps.

(1) Wave spectrum simulation

In this paper, the Elfouhaily spectrum [*Elfouhaily T et al., 1997*] is adopted to simulate the wave spectrum, and the time-varying ocean surface is simulated by the spectral model. The Elfouhaily spectrum is a full wavenumber spectrum that is based on the low-wavenumber Jonswap spectrum and the high-wavenumber Phillips spectrum [*Phillips, 1985*] and is more representative of the actual sea state. The key feature is the similarity between the description of high wavenumbers and low wavenumbers. Both forms emphasize the interaction of air with wind and waves. The direction function of the spectrum is symmetric with respect to the wind direction and has a correlation between wavenumber and wind speed. The low-wavenumber spectrum of the Elfouhaily spectrum is expressed as:

$$B_l = \frac{\alpha_p}{2} \cdot \frac{c_p}{c} \cdot F_p \tag{1}$$

where α_p is the equilibrium range parameter for long waves, c_p is the phase velocity corresponding to the peak wavenumber, and F_p is the long-wave side effect function. The high-wavenumber spectrum of the Elfouhaily spectrum is expressed as:

$$B_h = \frac{\alpha_m}{2} \cdot \frac{c_m}{c} \cdot F_m \tag{2}$$

where α_m is the equilibrium range parameter for short waves, c_m is the minimum phase velocity, and F_m is the short-wave side effect function. The full wavenumber spectrum is expressed as:

$$S = k^{-3}(B_l + B_h) \tag{3}$$

The direction function formula is as follows:

$$f(k,\varphi) = \frac{1}{2\pi}\left[1+\Delta(k)\cos(\varphi)\right] \tag{4}$$

$$\Delta(k) = \tanh[a_0 + a_p(\frac{c}{c_p})^{2.5} + a_m(\frac{c_m}{c})^{2.5}] \tag{5}$$

$$a_0 = \frac{\ln(2)}{4} = 0.1733;\ a_p = 4;\ a_m = 0.13\frac{U_f}{c_m} \tag{6}$$

The wavenumber direction spectrum can be represented by the full wavenumber spectrum and direction function as follows:

$$E(k, \varphi)=S f(k, \varphi)/k \tag{7}$$

(2) Ocean surface simulation

After completing the wave spectrum simulation, this paper adopts a linear filtering method to simulate the 2D ocean surface. The specific steps of simulation are as follows: First, 2D Gaussian white noise is generated in the frequency domain. Then, the Gaussian white noise is linearly filtered by the wave spectrum, and an inverse Fourier transform (IFFT) is performed to obtain the ocean surface height distribution. At any time t, the Fourier transform (FFT) component of the frequency domain can be expressed in terms of [*Xu X. J., 2013*]:

$$A_L(\vec{k},t) = \pi G(\vec{k}) \cdot \sqrt{2L_xL_yS_E(k,\varphi)}e^{j\omega(k)\cdot t} + \pi G^*(-\vec{k}) \cdot \sqrt{2L_xL_yS_E(k,\pi-\varphi)}e^{-j\omega(k)\cdot t} \tag{8}$$

where $\vec{k}$=(k_x, k_y) represents the ocean surface wavenumber vector, L_x and L_y are the lengths of the 2D ocean surface in the x- and y-axis directions, respectively, $G(\vec{k})$ is a 2D random number from a complex Gaussian distribution with a mean of 0 and a variance of 1, and $G^*(-\vec{k})$ is the inverse conjugate of $G(\vec{k})$. Since the linear filtering method simulates the generation of a "freezing ocean surface", the time t is set to 0 during the simulation. Performing an IFFT on $A_L(\vec{k}, t)$ can generate a linear ocean surface as follows:

$$\eta_L(\vec{r},t) = \frac{1}{L_xL_y}\sum\sum A_L(\vec{k},t)\exp(i\vec{k}\cdot\vec{r}) \tag{9}$$

where $\eta_L(\vec{r}, t)$ represents the ocean surface height at time t and position $\vec{r}$. To make η_L real, the following relationship needs to be satisfied:

$$\begin{aligned} A_L(k_x,k_y) &= A_L^*(-k_x,-k_y) \\ A_L(k_x,-k_y) &= A_L^*(-k_x,k_y) \end{aligned} \tag{10}$$

(3) Calculation of the backscattering coefficient

The incidence angle range of SAR is mostly 20°-60°. An SAR electromagnetic wave has resonance scattering with the ocean surface in the medium range. Ocean surface backscattering is

caused by Bragg scattering [*Kudryavtsev et al., 2005*]. Therefore, the accuracy of the calculation of the backscattering coefficient determines the accuracy of SAR imaging data. In this paper, a two-scale electromagnetic scattering model is used to calculate the backscattering coefficient, and the SAR polarization mode is defined as VV polarization. The backscattering coefficient can be expressed as [*Yoshida and Rheem, 2013*]:

$$\begin{aligned} \sigma_{BVV}^{0}(\theta) &= 8k^4 \cos^4\theta \,|U_{VV}|^2 \, S(2k\sin\theta, 0) \\ U_{VV} &= \frac{(\varepsilon-1)[\sin^2\theta - \varepsilon(1+\sin^2\theta)]}{[\varepsilon\cos\theta + \sqrt{\varepsilon - \sin^2\theta}]^2} \end{aligned} \tag{11}$$

where θ is the SAR incidence angle, k is the number of electromagnetic waves emitted by the SAR, and U_{VV} is the vertical polarization factor.

(4) Generation of echo signals

The algorithms for simulating echo signals are divided into a time-domain algorithm and a frequency-domain algorithm. The time-domain algorithm simulates the real working process of SAR and can acquire the original echo signals. Although the amount of calculation is large, the generated echo signals are the most accurate. Therefore, the time-domain algorithm is selected in this paper to simulate the echo signals. The echoes of K point targets can be obtained by superposition, as shown in equation (1). It should be noted that the point targets have no height, but the simulated ocean surface does. Therefore, the ocean height should be taken into account in the calculation of echo signals as follows:

$$\begin{aligned} Sr(n,m) &= \sum_{k=1}^{K} \sigma \cdot \exp\{j\pi[t(m) - \frac{2R(n;k)}{C}]\} \cdot \exp[-j\frac{4\pi}{\lambda}R(n;k)] \\ 0 < [t(m) - \frac{2R(n;k)}{C}] < Tr; &|\, R(n;k) - x(k) \,| < Tsar \\ n = 1,2,3\cdots N; &\, m = 1,2,3\cdots M \end{aligned} \tag{12}$$

where C is the speed of light, σ is the backscattering coefficient, $R(n; k)$ is the slant distance, $Tsar$ is the SAR integration time, and Tr is the pulse duration.

(5) Simulation of synchronization data

The echo signals are processed by the Range-Doppler (RD) imaging algorithm to obtain the ocean surface SAR images. The SAR that implements the imaging simulation is named SAR-1. Based on the parameters and working principle of SAR-1, two other SARs with angles of 10 °and 20 °to the flight direction of SAR-1 are simulated and are named SAR-2 and SAR-3, respectively. The orbits of SAR-2 and SAR-3 are obtained by counterclockwise rotation of the orbits of SAR-1. The premise of simulating a satellite is to ignore the Earth's rotation and ground bending. The difficulty lies in adjusting the position coordinates of subsatellite points according to the SAR's orbital parameters and ensuring the angles between the tracks of the three SARs. The three SARs operate in the form of satellite networks, enabling simultaneous observation of the same ocean area and synchronization of SAR ocean wave data. A schematic diagram of the three SAR observations in the same ocean is shown in Figure 1. Some parameters of the SAR system are shown in Table 1.

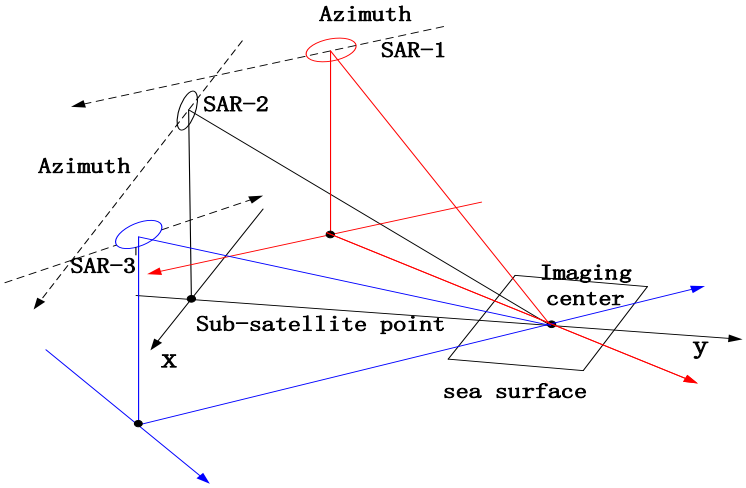

Figure 1. Networked SAR satellite observations of the same ocean.

Table 1. System parameters.

Parameters	Value	Parameters	Value
Platform height	530 km	Orbital semi-major axis	6901 km
Speed	7600 m/s	Orbital flattening	0.003
Observation angle of incidence	30 °	Orbital inclination	97.423 °
Carrier frequency	9.5 GHz	Right ascension	60
Pulse duration	10 μs	Perigee amplitude Angle	160
Chirp frequency modulation bandwidth	100 MHz	The moment of flight ascending node	0

2.2 MPI wave spectrum inversion method

SAR imaging of swells can generally be approximated by linear approximations. However, in the case of wind waves, nonlinearity becomes very important. Hasselmann derived the following nonlinear transformation relationship between the SAR image spectrum and the wave direction spectrum:

$$P^S(k)=\frac{1}{4\pi^2}\exp(-k_x^2\xi'^2)\cdot\int\exp(-k_x^2\xi'^2\langle v^2\rangle^{-1}f^v(\mathrm{r}))\cdot \{1+f^R(\mathrm{r})+ik_x\beta(f^{Rv}(\mathrm{r})-f^{Rv}(-\mathrm{r})) +k_x^2\beta^2[f^{Rv}(\mathrm{r})-f^{Rv}(0)][f^{Rv}(-\mathrm{r})-f^{Rv}(0)]\}dr\,\mathrm{e}^{-ikr} \tag{13}$$

where

$$f^R(r)=0.5\int(F(k)|T_k^R|^2+F(-k)|T_{-k}^R|^2)\exp(ikr)dk \tag{14}$$

$$f^v(r)=\int F(k)|T_k^v|^2\exp(ikr)dk \tag{15}$$

$$f^{Rv}(r)=0.5\int(F(k)T_k^R(T_k^v)^*+F(-k)T_{-k}^v(T_{-k}^R)^*)\exp(ikr)dk \tag{16}$$

The above three formulas correspond to the autocorrelation of SAR image intensity, the autocorrelation of velocity along the track direction, and the correlation of the two, respectively. The MPI algorithm for inverting the wave spectrum is derived based on the nonlinear transformation relationship. The MPI algorithm describes the mapping relationship between an ocean wave

spectrum and SAR image spectrum. In the process of inversion, it is necessary to overcome the information loss caused by the 180 ° mapping ambiguity and azimuth cutoff. The idea of the algorithm is to introduce the first-guess wave spectrum, construct the value function, and output the optimal wave spectrum and the optimal SAR spectrum after minimizing the value function through iteration.

3. Estimation of the azimuth cutoff and wave spectrum data fusion method

3.1 Estimation of the azimuth cutoff and analysis of influencing factors

The azimuth cutoff is a measure of SAR's azimuth observation ability. The nonlinear effect of velocity bunching modulation is the main cause of the azimuth cutoff. Affected by the additional speed, if the ratio of the displacement of the image to the long wavelength is small, the effect is linear; the effect is nonlinear if the displacement of the image is greater than or equal to the wavelength. This nonlinear modulation applies only to waves propagating in the azimuth direction. The reason is that SAR achieves high azimuth resolution through synthetic aperture in azimuth and pulse compression in range, while the principle of synthetic aperture is realized based on the Doppler effect. The function of velocity bunching modulation is shown in Figure 2. When a wave propagates in the azimuth direction, the area in front of the crest produces an upward additional velocity, resulting in a positive Doppler shift. The scattering target moves in the positive direction of the azimuth in the SAR image, and the scattering bins gather near the trough, making the trough brighter and the crest darker. If a downward additional velocity is generated behind the wave peak, the scattering target moves in the negative direction of the azimuth in the SAR image. The SAR wave image will have a darker trough and a brighter crest. The magnitude of the displacement is $d = \beta * u_r$, where β is the range-to-velocity ratio and u_r is the radial velocity component toward the radar. This displacement causes the SAR image to be blurred in the azimuth direction, and the wave information having a wavelength smaller than the cutoff wavelength is lost. In addition to velocity bunching modulation, there is another factor that produces azimuth cutoff. Due to the limited time of the scatterer, the coherence time of the wave scene is less than the SAR acquisition time, which leads to azimuth cutoff as follows:

$$T = \frac{R\mu}{V_f} \tag{17}$$

where R refers to the slant range of the SAR to the imaging target and μ refers to the azimuth beamwidth of the antenna pattern. For spaceborne SAR, V_f stands for the antenna pattern footprint velocity across the Earth's surface; for airborne SAR, V_f is considered to be the same speed as the platform velocity in orbit [*Vachon et al., 1994*].

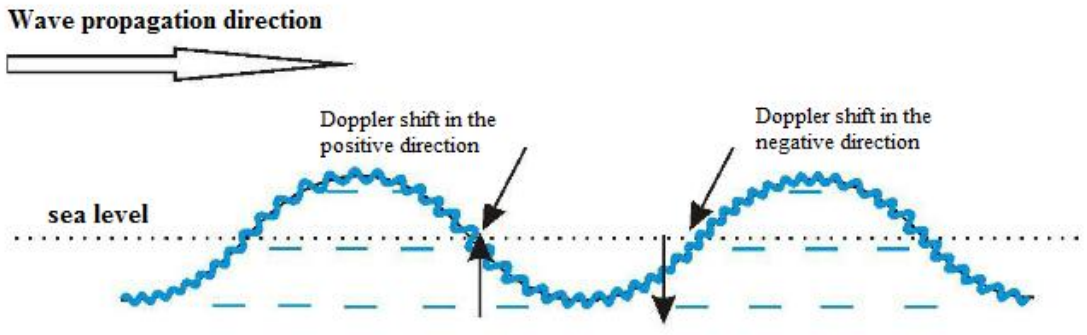

Figure 2. Schematic diagram of velocity bunching modulation.

There is no clear expression for the calculation of the azimuth cutoff, so the cutoff wavelength value can be obtained by estimation. In 1983, Beal first proposed an empirical formula for estimating the azimuth cutoff. The formula simply uses the range-to-velocity ratio and the effective wave height to estimate the cutoff wavelength. However, in addition to the significant wave height, wind speed, wave orbital velocity, etc., all have an effect on the azimuth cutoff. A variety of methods for estimating the azimuth cutoff have emerged through research. The method used for estimating the cutoff wavelength in this paper is shown in equation (18). This method is based on the hypothesis of linear waves [*Lyzenga, 1986*], considering the line-of-sight orbital velocity rather than the vertical velocity [*Kerbaol, 1998*]:

$$\lambda_c = \pi\beta\sqrt{\int |\mathrm{T}_k^v|^2 \, F(k)\mathrm{d}k} \tag{18}$$

where,

$$T_k^v = -\omega(\sin\theta\frac{k_r}{|k|} + \mathrm{i}\cdot\cos\theta) \tag{19}$$

where ω is the angular frequency, θ is the SAR incidence angle, k_r is the component of the wavenumber in the range direction, k is the wavenumber, and T_k^v is range velocity transfer function. $S(k)$ is the optimum wave spectrum obtained by inversion using the MPI algorithm.

The azimuth cutoff is related to the significant wave height, wind speed, range-to-velocity ratio, SAR incidence angle and wave propagation direction. In this paper, the relationship between the wave parameters and the azimuth cutoff is studied based on the processed 24 ASAR and Radarsat-2 measured data. The basic information of the 24 scene data is shown in Table 2. The variables included in the SAR data are significant wave height, wind speed, wavenumber spectrum, etc.

Table 2. Basic information of 24 scene SAR measured data

Name of SAR data	Time	Latitude and longitude range
ASA_IMS_1PNDPA20101012_021940_ 000000162093_00404_45047_0301	2010.10.12 02:19:48	38.9 °N – 40.1 °N 118.5 °E- 120.1 °E
ASA_IMS_1PNDPA20101012_021953_ 000000162093_00404_45047_0294	2010.10.12 02:20:01	38.15 °N – 39.33 °N 118.38 °E- 119.86 °E
ASA_IMS_1PNDPA20101012_022007_ 000000162093_00404_45047_0295	2010.10.12 02:20:15	37.3947 °N - 38.4869 °N 120.2619 °E- 121.705 °E
ASA_IMS_1PNIPA20110730_021919_ 000000163105_00075_49227_0084	2011.07.30 02:19:27	37.31 °N - 38.49 °N 118.16 °E- 119.62 °E
ASA_IMS_1PNIPA20110730_021933_ 000000163105_00075_49227_0083	2011.07.30 02:19:41	38.01 °N – 39.12 °N 118.38 °E- 119.54 °E
ASA_IMS_1PNUPA20090419_133817_ 000000162078_00182_37310_0161	2009.04.19 13:38:25	37.5 °N - 38.68 °N 120.59 °E- 122.06 °E
ASA_IMS_1PNUPA20090419_133831_ 000000162078_00182_37310_0173	2009.04.19 13:38;39	38.33 °N – 39.51 °N 120.35 °E- 121.84 °E
ASA_IMS_1PNUPA20090419_133845_ 000000152078_00182_37310_0158	2009.04.19 13:38:53	39.17 °N – 40.31 °N 120.12 °E- 121.61 °E
ASA_IMS_1PNUPA20100118_021109_ 000000162086_00089_41225_0165	2010.01.18 02:11:18	39.1 °N – 40.27 °N 120.14 °E- 121.61 °E

ASA_IMS_1PNUPA20100118_021124_000000162086_00089_41225_0166	2010.01.18 02:11:32	38.26 ℕ – 39.43 ℕ 119.92 ℇ- 121.38 ℇ
ASA_IMS_1PNUPA20100118_021138_000000162086_00089_41225_0167	2010.01.18 02:11:46	37.43 ℕ - 38.6 ℕ 119.7 ℇ- 121.14 ℇ
RS2_OK29469_PK291172_DK262911_S3_20120427_220254_VV_VH_SLC	2012.4.27 22:03:02	37.3947 ℕ - 38.4869 ℕ 120.2619 ℇ- 121.705 ℇ
RS2_OK29469_PK291175_DK265287_S5_20120504_215847_VV_VH_SLC	2012.05.04 21:58:55	37.3503 °N- 38.4314 ℕ 120.1911 ℇ- 121.6256 ℇ
RS2_OK29469_PK291177_DK265289_S5_20120507_095633_VV_VH_SLC	2012.05.07 09:56:41	37.3622 ℕ -38.4428 ℕ 120.2247 ℇ- 121.6606 ℇ
RS2_OK29469_PK291174_DK262913_S5_20120430_100011_VV_VH_SLC	2012.4.30 10:00:19	35.4572 °N- 36.5403 ℕ 119.6169 ℇ- 121.0189 ℇ
RS2_OK29469_PK291176_DK265288_S5_20120504_215921_VV_VH_SLC	2012.05.04 21:59:29	35.3692 ℕ- 36.4517 ℕ 119.7708 ℇ -121.1697 ℇ
RS2_OK29469_PK291178_DK265290_S1_20120507_221148_VV_VH_SLC	2012.05.07 22:11:56	35.4125 ℕ- 36.5097 ℕ 119.51 ℇ -120.8597 ℇ
RS2_OK29469_PK292895_DK262912_S3_20120427_220329_VV_VH_SLC	2012.04.27 22:03:37	35.3244 ℕ -36.4175 ℕ 119.7908 ℇ -121.1953 ℇ
RS2_OK31199_PK310675_DK277122_S3_20120725_095222_VV_SLC	2012.07.25 09:52:30	37.3694 ℕ- 38.4617 ℕ 120.1681 ℇ -121.6119 ℇ
RS2_OK31199_PK310676_DK277123_S4_20120727_224826_VV_SLC	2012.07.27 22:48:33	37.45 ℕ -38.6417 ℕ 120.2178 ℇ- 121.7642 °E
RS2_OK31199_PK310677_DK277124_S2_20120801_094812_VV_SLC	2012.08.01 09:48:21	37.345 ℕ -38.2531 ℕ 120.075 ℇ -121.5333 ℇ
RS2_OK31198_PK310678_DK277125_S2_20120725_220739_VV_SLC	2012.07.25 22:07:47	35.2486 ℕ -36.1567 ℕ 119.8289 ℇ -121.2444 ℇ
RS2_OK31198_PK310679_DK277126_S3_20120801_220330_VV_SLC	2012.08.01 22:03:38	35.2583 ℕ -36.3514 ℕ 119.7767 ℇ -121.18 ℇ
RS2_OK31198_PK310931_DK277277_S3_20120708_220330_VV_SLC	2012.07.08 22:03:37	35.2592 ℕ -36.3519 ℕ 119.7761 ℇ -121.1797 ℇ

Taking Envisat ASAR data ASA_IMS_1PNIPA20110730_021919_000000163105_00075_49227_0084.N1 as an example, 10 small areas with obvious wave information were selected to estimate the corresponding azimuth cutoff for each small area and obtain SAR parameters such as SAR incidence angle, platform velocity and platform height. A schematic diagram of the angle between the azimuth and north is shown in Figure 3. The horizontal and vertical axes in the figure are the range direction and the azimuth direction, respectively, and the black arrow points to the north. The parameters extracted by these data are shown in Table 3.

Table 3. Various parameters of ASAR data extraction

Azimuth cutoff (m)	Significant wave height (m)	Wind speed (m/s)	SAR incident angle (°)	Wave propagation direction (°)	angle between azimuth and north (°)	Azimuth angle (°)
120.931	0.82	6.047	26.5971	180		11.5
101.462	0.8	4.386	26.2916	280		-88.5

173.2293	1.158	4.15	27.2147	280	168.5	-88.5
389.6311	3.6	7.52	28.0946	285		-93.5
171.206	1.31	5.036	27.2159	280		-88.5
555.6558	4.99	8.117	28.0958	285		-93.5
100.6521	0.802	7.445	28.3843	320		-128.5
50.0034	0.626	10.536	26.3098	310		-118.5
126.604	1.519	11.531	28.1058	200		-20
174.2902	1.36	12.58	28.3887	95		96.5

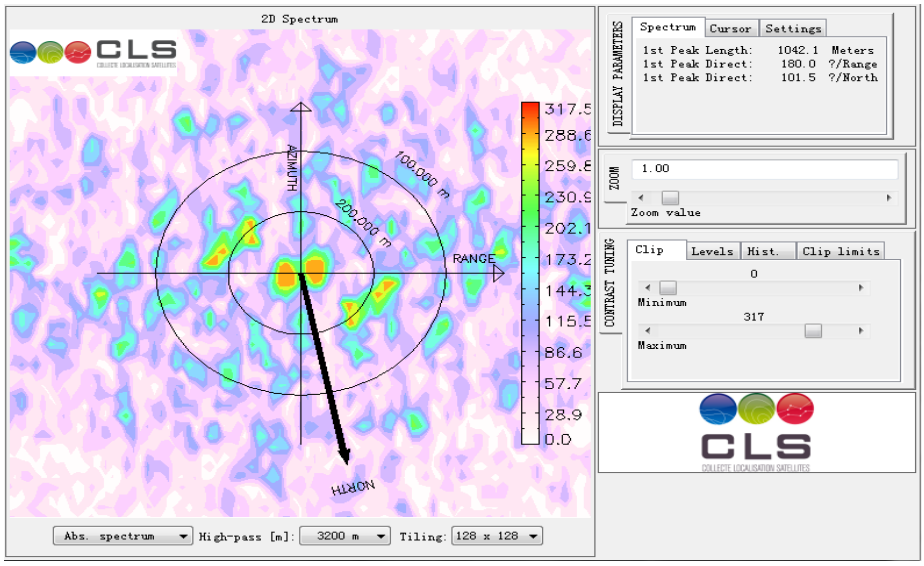

Figure 3. Schematic diagram of the orientation between the azimuth and north.

After extracting the wave parameters of the 24 SAR data, the significant wave height, wind speed and azimuth angle are independent variables, and the azimuth cutoff is the dependent variable; the relationships between the independent variables and the dependent variable are analyzed by the method of linear regression. The relationships obtained by this fitting are as follows:

(1) The regression equation between the azimuth cutoff and significant wave height is y=43.063+42.3482x, and the correlation coefficient is 0.6343.

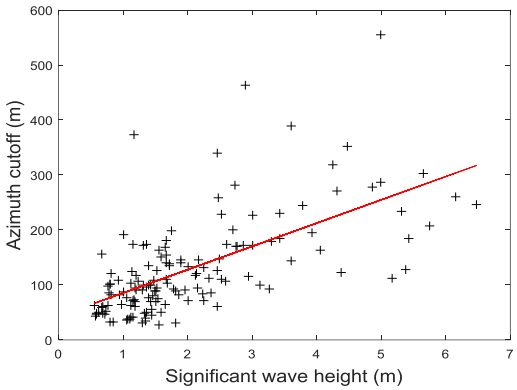

Figure 4. The result of fitting the azimuth cutoff to the significant wave height.

(2) The regression equation between the azimuth cutoff and wind speed is y=75.8845+8.2724x, and the correlation coefficient is 0.4564.

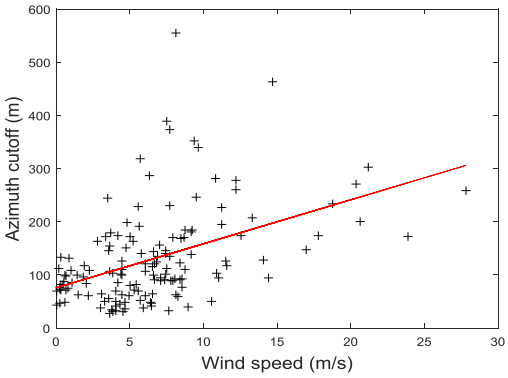

Figure 5. The result of fitting the azimuth cutoff to the wind speed.

(3) The result of fitting the azimuth cutoff to the azimuth angle is not relevant.

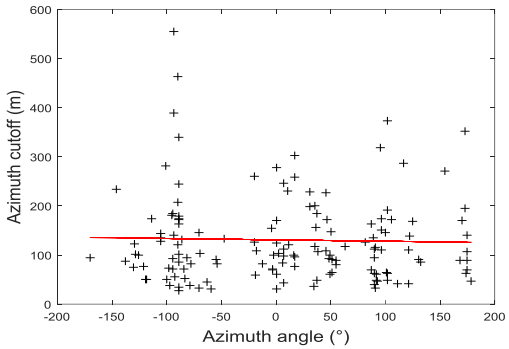

Figure 6. The result of fitting the azimuth cutoff to the azimuth angle.

As shown in the results, in the case of a relatively large significant wave height, regardless of the magnitude of the wind speed, the corresponding azimuth cutoff is relatively large. In the case where the significant wave height is relatively small, even if the wind speed is relatively large, the azimuth cutoff is relatively small. The effect of significant wave height on the azimuth cutoff occurs in all growth states of the ocean wave. When the wind speed is large, the cutoff wavelength is only large when the significant wave height is large, indicating that the correlation between the azimuth cutoff and the wind speed only has a great influence on the fully grown sea state. The above analysis also reflects the degree of azimuth cutoff in the case of wind waves and swells. In the case of swells, even if there is no wind, the significant wave height may be large, and the corresponding azimuth cutoff will be large. In the case of wind waves, the higher the wind speed is, the higher the significant wave height and the larger the azimuth cutoff. Moreover, in the case where the factors affecting the azimuth cutoff are not equal, the relationship between the azimuth cutoff and the azimuth angle cannot be explored. This relationship needs to be obtained through simulation SAR wave data.

3.2 Wave spectrum data fusion method

In this paper, the wave data fusion method is adopted in the study of the SAR wave cutoff wavelength compensation method. First, the MPI method is used to extract a single SAR wave spectrum, and the relationship between the azimuth angle and the azimuth cutoff is studied. Then, based on this relationship, a multiview wave spectrum data fusion method is established. Finally, the multiview wave spectrum data are fused, the azimuth cutoff compensation method is established, and the compensation effect is verified. Wave data fusion is the basis for modeling the azimuth cutoff compensation method. Before establishing the wave spectrum data fusion method, the influence of different wave propagation directions on the azimuth cutoff should be clarified. In the

case where the wave propagation direction is at an angle to the SAR flight direction (azimuth direction), the degree of intensity of the azimuth cutoff of the SAR observation wave is different. Claus pointed out in the literature that in a strongly nonlinear imaging scheme, the velocity bunching mechanism causes the peaks to rotate toward the range direction [*Claus et al., 1990*]. Nonlinear imaging distortion is strongest for broad spectra (wind waves) and weak for narrowband swells. In linear and weakly nonlinear imaging schemes, the superposition of hydrodynamic and tilt cross-section modulation with the velocity bunching transfer function typically produces a rotation of the spectral peak toward the azimuth direction. The interference characteristics of different modulation mechanisms depend on the wave propagation direction, and the wave propagation direction is an important factor affecting the azimuth cutoff. Therefore, the relationship between the azimuth angle and the azimuth cutoff is the basis for establishing a multiview SAR wave spectrum data fusion method.

The spectral data simulated by the E spectrum are used as *S(k)*. According to equation (18), when the parameters such as φ_0 and range-to-velocity ratio are fixed, the SAR incidence angle θ is changed, and it is found that the azimuth cutoff increases as the incidence angle of SAR increases, as shown in Figure 7a. When the SAR incidence angle is fixed, only φ_0 is changed, and it is found that the larger that φ_0 is, the smaller the cutoff wavelength value, as shown in Figure 7b. The azimuth angle and φ_0 are mutual relations, and it can be inferred that the azimuth angle is proportional to the cutoff wavelength. All angles are defined as angles to the positive direction of the azimuth and range direction. The azimuth angles of the three SAR data are 45 °, 55 °, and 65 °, respectively. The cutoff wavelengths of the data calculated according to equation (18) are 156.95 m, 158.56 m, and 159.96 m, respectively. The correlation between the azimuth angle and the azimuth cutoff for the three SAR data confirms the correctness of the above conclusions.

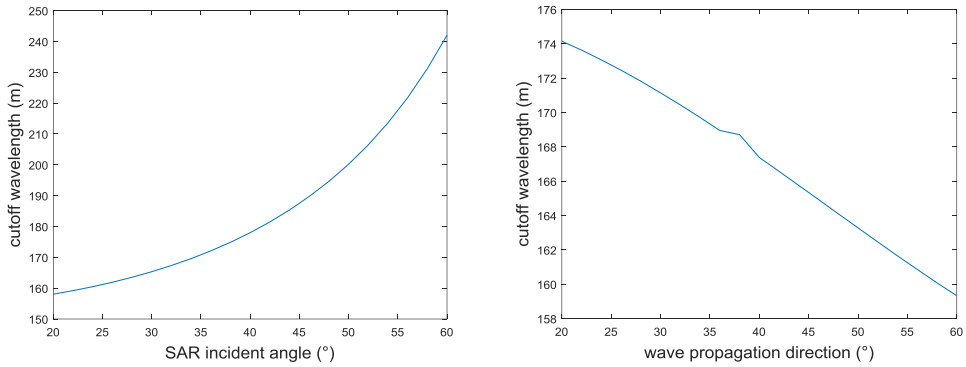

Figure 7. (a) The relationship between the azimuth cutoff and the incident angle; (b) the relationship between the azimuth cutoff and φ_0.

Based on this, a wave data fusion method is established. The detailed technical route of the method is shown in Figure 8.

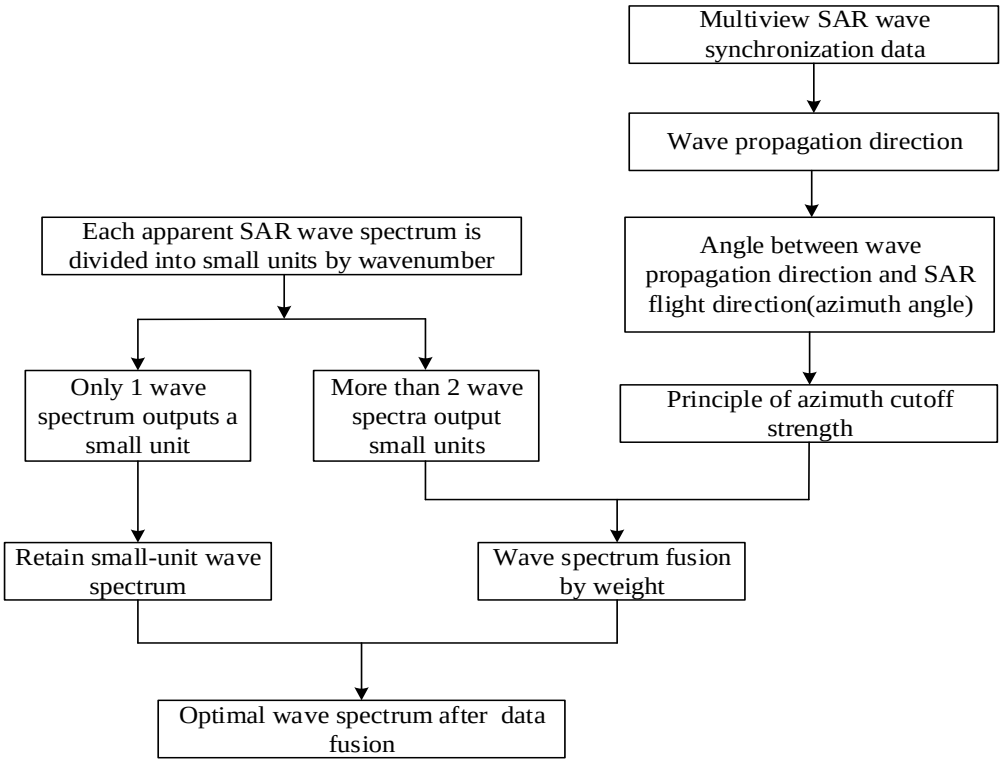

Figure 8. Flow chart of multiple-SAR wave spectrum data fusion technology.

The specific research plan is as follows:

(1) Defining the azimuth angle of each single SAR;

(2) Determining the data fusion weights of different azimuth angles;

(3) The wave spectrum obtained by inversion of a single SAR is divided into small units according to the wavenumber interval of the azimuth direction and the distance direction, and whether there is an output wave spectrum result is judged for each small unit. If a small unit has only 1 wave spectrum output result, the output of the small unit is retained; if a small unit corresponds to more than 2 wave spectra output results, the output wave spectrum is fused according to the determined wave spectrum fusion weight.

The determination of the fusion weight should follow the principle that the sum of the weights is less than 1. According to the regular pattern that the azimuth cutoff decreases with the azimuth angle, the method of determining the fusion weight based on the quadrant is established. When the sum of the azimuth angles is in the range of 0 °-90 °, the fusion weight is determined to be the ratio of the azimuth angle to 90 °. Additionally, when the sum of the azimuth angles is in the range of 90 °-180 °, the fusion weight is determined to be the ratio of the azimuth angle to 180 °, when the sum of the azimuth angles is in the range of 180 °-270 °, the fusion weight is determined to be the ratio of the azimuth angle to 270 °, and when the sum of the azimuth angles is in the range of 270 °-360 °, the fusion weight is determined to be the ratio of the azimuth angle to 360 °. After determining the fusion weight, the MPI algorithm is used to invert the SAR wave data, and the wave spectrum is merged to estimate the azimuth cutoff before and after the fusion.

4. Results and discussion

4.1 Results of multiview SAR wave synchronization data

Ocean surface simulation provides a background field for the calculation of the backscattering

coefficient. When the background field is constructed, the simulated SAR can emit electromagnetic waves and receive echoes, and then the backscattering coefficient is calculated in combination with the electromagnetic scattering model. Therefore, the accuracy of the constructed ocean surface directly determines the accuracy of the calculation of the backscattering coefficient. The linear filtering method is mainly based on the FFT and has the characteristics of faster calculation speed and more obvious ocean surface detail features. The 2D ocean surface simulated by the linear filtering method is the observation target. This paper simulates virtual networked satellites with three SARs and simulates the SAR synchronous observation data of different orbit directions by networked cooperative observation. The ocean surface and backscattering coefficients obtained from observations by SAR and the corresponding ocean SAR images are shown in Figures 9-11.

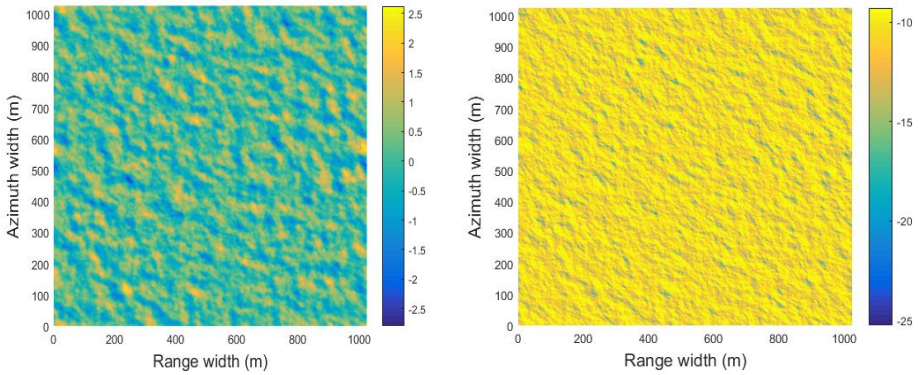

(a) (b)

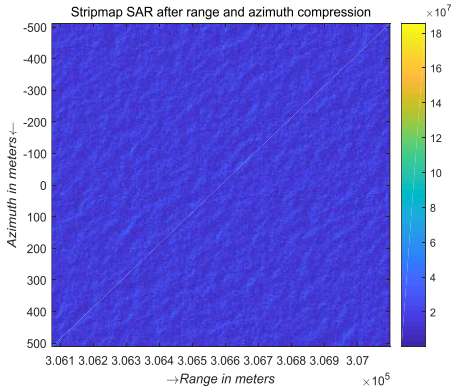

(c)

Figure 9. Data observed by SAR-1 as follows: (a) ocean surface, (b) backscattering coefficient, and (c) ocean SAR image.

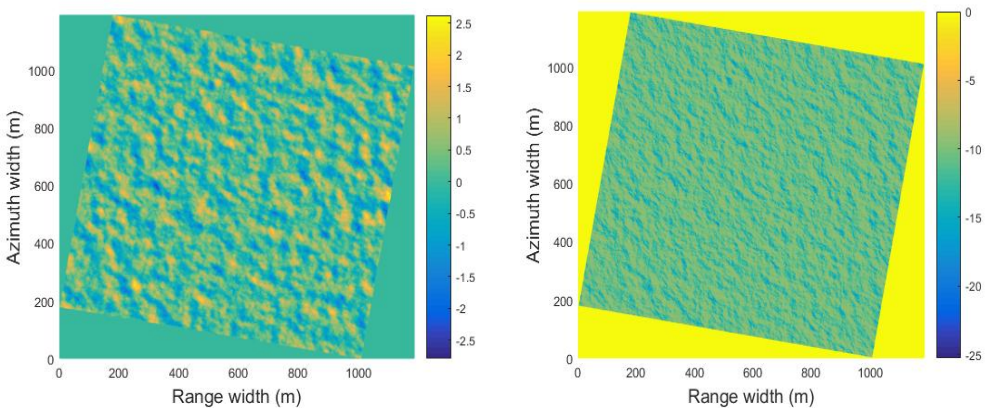

(a) (b)

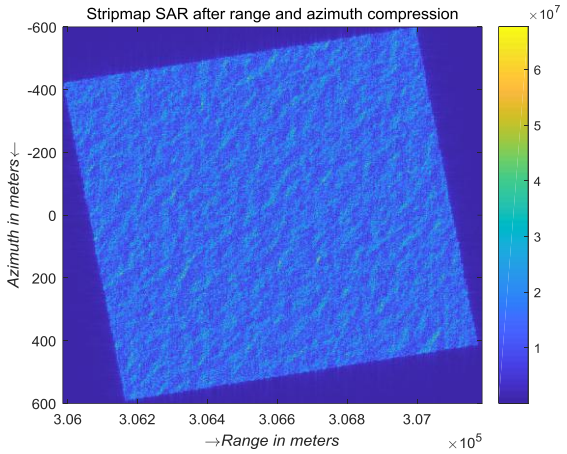

(c)

Figure 10. Data observed by SAR-2 as follows: (a)ocean surface, (b) backscattering coefficient, and (c) ocean SAR image.

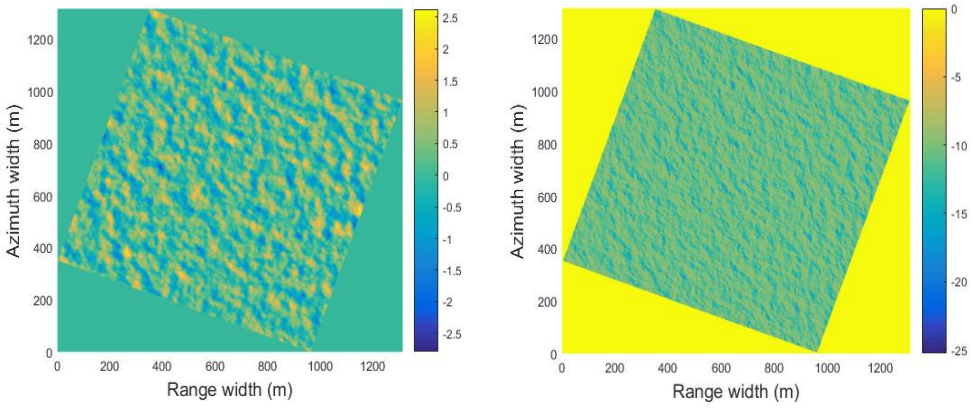

(a) (b)

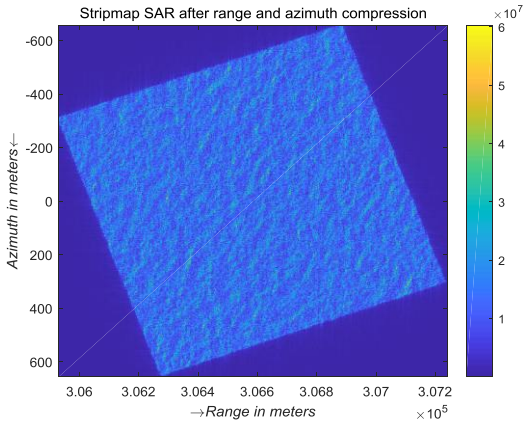

(c)

Figure 11. Data observed by SAR-3 as follows: (a)ocean surface, (b) backscattering coefficient, and (c) ocean SAR image.

The method for calculating the backscattering coefficient is based on the simulated ocean surface,

and the slope of the ocean surface is obtained to avoid the probability density function of the artificially assumed slope. In the figures, the fringes of the ocean surface and the backscattering coefficient tend to be consistent, and the backscattering coefficient of VV polarization is mainly distributed between -10 dB and -15 dB. The results in the figures are consistent with the conclusions in the existing literature [*Ward et al., 2013*], indicating that the calculated backscattering coefficient is accurate. In the simulation process, the RD algorithm performs FFTs and IFFTs on the azimuth and range of the echo signals, respectively, which causes the ocean SAR image to be horizontally symmetrical with the ocean surface and backscattering coefficient.

4.2 Wave spectrum inversion of synchronous data

After simulating the multiview SAR synchronization data, the MPI algorithm is used to process the SAR wave data obtained by SAR-1 observations. The accuracy of the inversion results can also verify the correctness of the simulated SAR data in Section 4.1. The inversion results of SAR data acquisition from SAR-1 are shown in Figure 12:

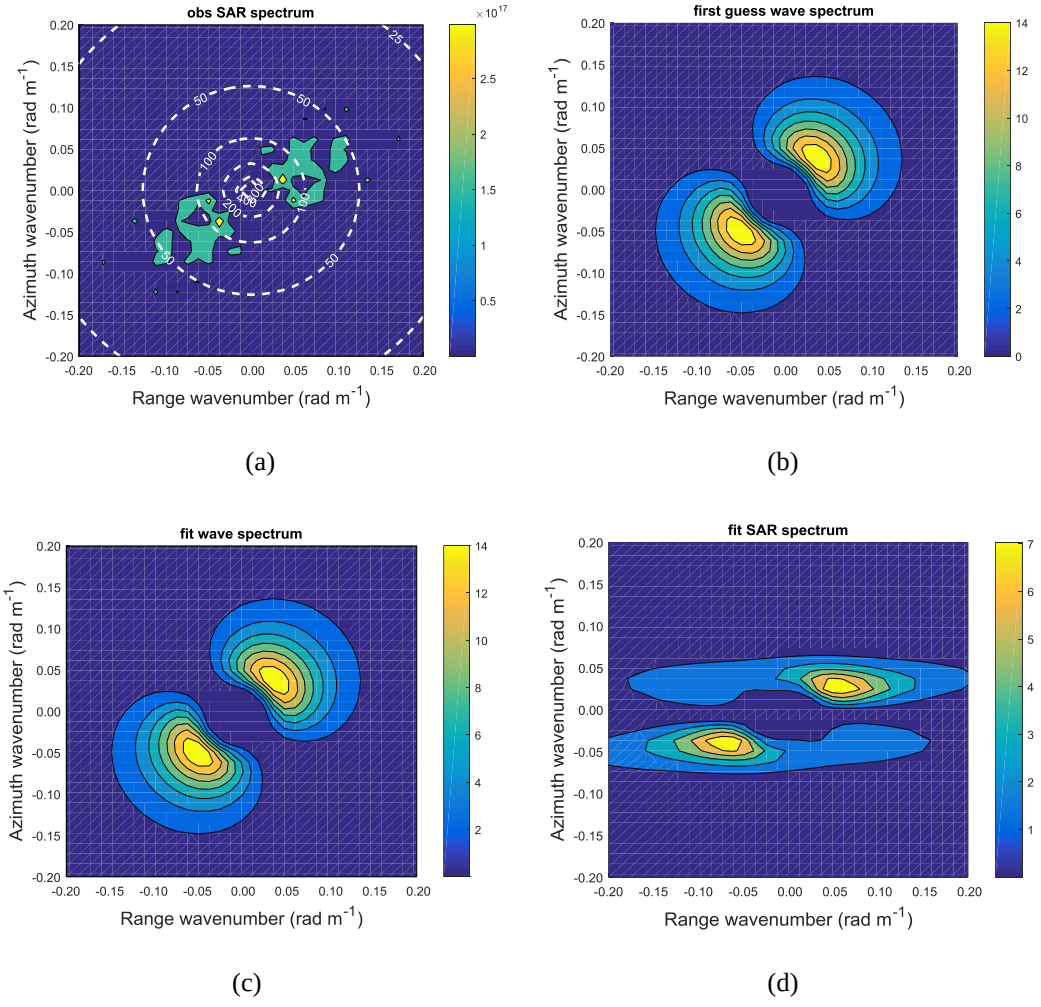

Figure 12. Results of SAR-1 wave spectrum inversion as follows: (a) observed SAR spectrum, (b) first-guess wave spectrum, (c) optimal wave spectrum, and (d) optimal SAR spectrum.

For SAR-2, the wave propagation direction is the same as that of SAR-1, which is 45 °. The orbital angle between SAR-1 and SAR-2 is 10 °. Since the included angle is obtained by rotating counterclockwise, we can calculate that the included angle between the wave propagation direction and the SAR-2 range direction is 35 °. The inversion results of SAR data acquisition from SAR-2

are shown in Figure 13:

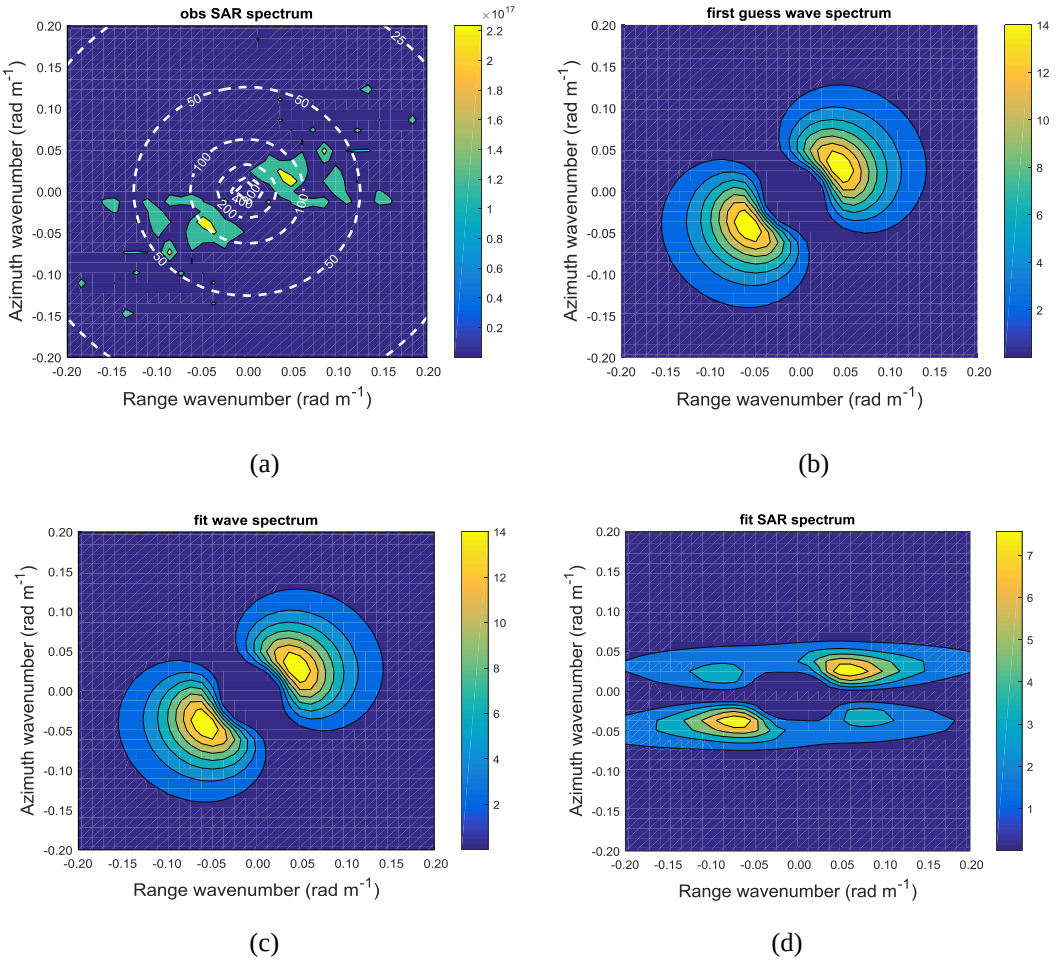

Figure 13. Results of SAR-2 wave spectrum inversion as follows: (a) observed SAR spectrum, (b) first-guess wave spectrum, (c) optimal wave spectrum, and (d) optimal SAR spectrum.

The orbital angle between SAR-1 and SAR-3 is 20 °, and the angle between the wave propagation direction and the distance is calculated to be 25 °. The inversion results of SAR data acquisition from SAR-3 are shown in Figure 14:

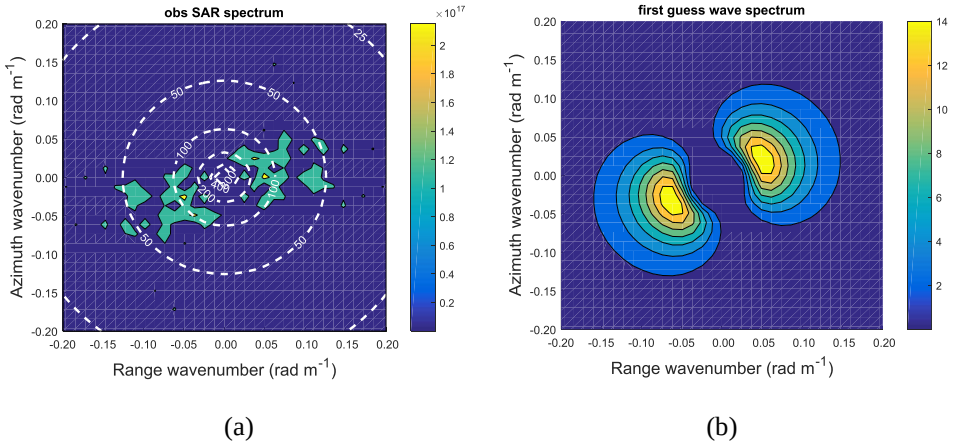

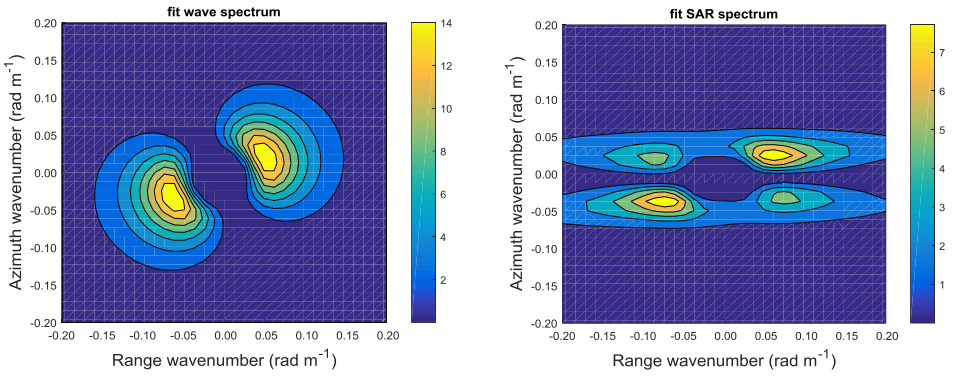

(c) (d)

Figure 14. Results of SAR-3 wave spectrum inversion as follows: (a) observed SAR spectrum, (b) first-guess wave spectrum, (c) optimal wave spectrum, and (d) optimal SAR spectrum.

Figures 12, 13, and 14 show that the shape and magnitude of the initial wave spectrum and the optimum wave spectrum are the same. It can be seen from the value function that the closer the initial guess spectrum is to the optimum wave spectrum, the better the inversion effect. It should be noted that the results of the observed SAR spectra are obtained by horizontal inversion. It can be seen from the optimum SAR spectrum that the spectrum is compressed in the azimuth direction. Only waves with wavelengths smaller than a certain threshold are imaged (the low-wavenumber waves are imaged, and the high-wavenumber waves are truncated), and this particular threshold is the azimuth cutoff. The influence of the azimuth cutoff on SAR imaging can be seen from the optimal SAR spectrum.

4.3 Multiple-SAR spectral data fusion and cutoff wavelength compensation

After obtaining the wave spectrum, the wave spectrum is fused according to the established data fusion method. The total azimuth angle of the three SAR data is 165 °, so the fusion weights are set to the ratio of each azimuth angle to 180 °. The fused formula is shown in equation (20). The results before and after the fusion are shown in Figure 15.

$$WS_{\mathrm{df}} = \frac{45 \cdot WS_1}{180} + \frac{55 \cdot WS_2}{180} + \frac{65 \cdot WS_3}{180} \tag{20}$$

where WS_1, WS_2, and WS_3 represent the wave spectra obtained from the single-SAR data inversion and WS_{df} indicates the wave spectrum after data fusion.

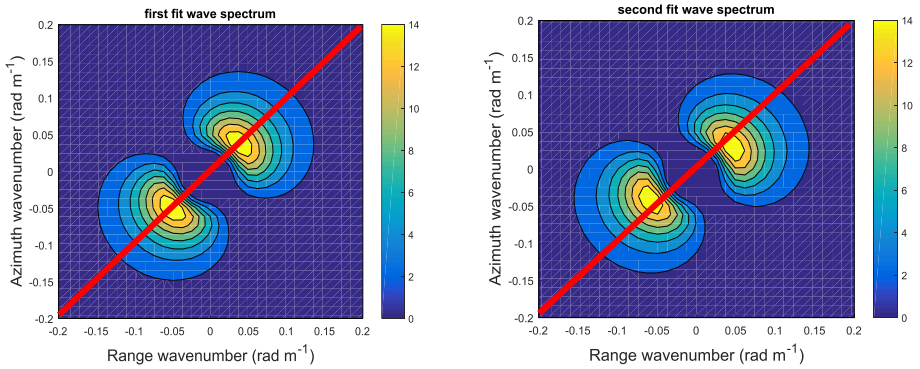

(a) (b)

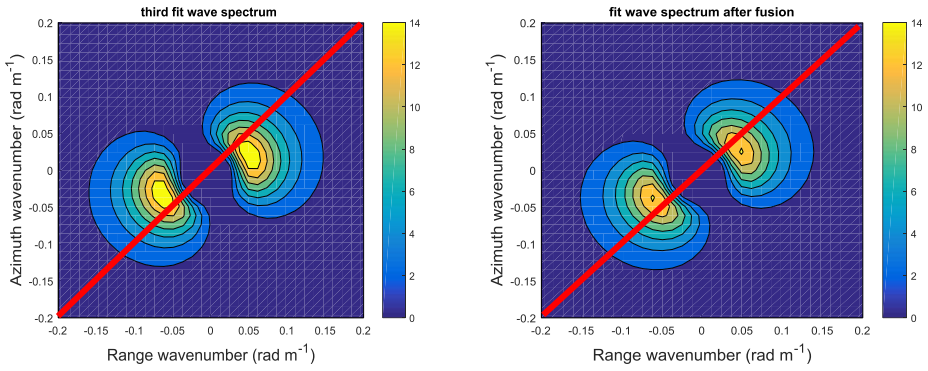

(c) (d)

Figure 15. The optimal wave spectra before and after data fusion. (a), (b), and (c) show the optimal wave spectra for three SAR data, and (d) shows the optimal wave spectrum after data fusion.

The effect of azimuth cutoff compensation is ultimately verified by the significant wave height and the mean wave period. It is generally believed that the root mean square error of the significant wave height and the true value of the significant wave height obtained by the inversion is less than 0.5 m, and the root mean square error of the mean wave period is less than 1.2 s, which is the index requirement in the field of ocean wave observation. To facilitate evaluation of the accuracy of the inversion wave parameters, it is necessary to provide a true effective wave height, where the effective wave height is estimated using the wind speed as follows:

$$H_s=0.0214\ U_{19.5}^2 \tag{21}$$

where $U_{19.5}$ represents the wind speed at a height of 19.5 m above sea level. However, in the process of wave calculation, the wind speed at a height of 10 m above the sea surface is usually taken for calculation. The conversion relationship between these wind speeds is shown in equation (22) [*Xu X. J., 2013*]:

$$U_h = U_{10}\bullet(1+2.5\lg(\frac{h}{10})(\sqrt{0.0015/[1+\exp\left(-\frac{U_{10}-1.25}{1.56}\right)]}+0.00104)) \tag{22}$$

The calculation formula for inverting the effective wave height is shown in equation (23). The wave spectrum is the optimum wave spectrum obtained by the MPI method.

$$H_s = 4\sqrt{m_0} = 4\sqrt{\int_0^{\infty}\int_0^{\infty} S(k_x,k_y)\,\mathrm{d}\,k_x\,\mathrm{d}\,k_y} \tag{23}$$

The calculation of the mean wave period (true value) is based on the significant wave period, and the significant wave period is calculated from the significant wave height. After calculating the significant wave period, the relationship between the mean wave period and the significant wave height is obtained based on the relationship between the significant wave period and the mean wave period. The expression is shown in equations (24-26).

$$\frac{gT_s}{2\pi U_{10}} = 3.31(\frac{gH_s}{U_{10}^2})^{\frac{3}{5}} \tag{24}$$

$$T_m = 0.74T_s \tag{25}$$

$$T_m = \frac{2\pi U_{10}}{g}\cdot 2.45\cdot(\frac{gH_s}{U_{10}^2})^{\frac{3}{5}} \tag{26}$$

The calculation formula of the inversion average wave period is as follows [*He W et al., 2012*]:

$$T_m = 2\pi\sqrt{\frac{m_0}{m_2}} = 2\pi\sqrt{\frac{\int_0^\infty\int_0^\infty S(k_x,k_y)\,\mathrm{d}k_x\,\mathrm{d}k_y}{\int_0^\infty\int_0^\infty g\sqrt{k_x^2+k_y^2}\cdot S(k_x,k_y)\,\mathrm{d}k_x\,\mathrm{d}k_y}} \tag{27}$$

The azimuth cutoff, significant wave height, and mean wave period before and after data fusion are shown in Table 4. The initial input conditions of the three SAR data are the same, and the significant wave height and mean wave period are the same. The results show that the azimuth cutoff after data fusion is smaller than that before fusion, indicating that the wave information observed by SAR after fusion is greater. The significant wave height before data fusion is 0.14 m compared with the input, and the mean wave period is 0.75 s compared with the input. The significant wave height after data fusion is 0.03 m compared with the input, and the mean wave period is 0.59 s compared with the input. The significant wave height and mean wave period after fusion are closer to the input values, indicating that the fusion results are more accurate and that the compensation results are effective.

Table 4. Comparison of wave parameters before and after data fusion

Optimal wave spectrum	SAR-1	SAR-2	SAR-3	After data fusion
Azimuth cutoff (m)	156.95	158.56	159.96	146.37
Azimuth angle (°)	45	55	65	
Input significant wave height (m)	2.27			
Inversion of significant wave height (m)	2.41			2.24
Input mean wave period (s)	6.15			
Inversion of mean wave period (s)	5.40			5.56

5. Conclusions

Based on simulation of multiview SAR wave synchronization data, this paper analyzes the influencing factors and compensation methods of the azimuth cutoff. The following conclusions can be drawn:

(1) In this paper, the time-domain echo algorithm is used to calculate the ocean surface echo signals. Although the calculation amount is large, the SAR data obtained by simulation have higher precision. The results of the MPI inversion demonstrate the effectiveness of the method.

(2) In the case where the parameters of the waves affecting the azimuth cutoff are different, the measured SAR data cannot be derived from the relationship between the azimuth angle and the azimuth cutoff. The wind speed and significant wave height of the simulation SAR wave data are all the same, and it can be concluded that the azimuth angle is positively proportional to the azimuth cutoff.

(3) The effect of the significant wave height on the azimuth cutoff occurs in all growth states of ocean waves. When the sea state is high, the wind speed will affect the azimuth cutoff.

(4) After the fusion of wave spectrum data, the significant wave height and mean wave period of the fused wave spectrum are more consistent with the input values. The azimuth cutoff decreased by 7.65%, which met the requirements of the observation index, indicating that the azimuth cutoff compensation method proposed in this paper is effective.

The work in this paper is based on simulation data, and verification is planned by measured data

in the future. The project cooperation unit has successfully developed SAR satellites and has planned to carry out SAR airborne flying tests, designing flight test experiments for different observation directions in the same ocean area. This approach is expected to obtain quasi-synchronized multiview SAR measured data and verify the effect of the azimuth cutoff wavelength compensation method.

Disclosure statement

No potential conflict of interest was reported by the authors.

Acknowledgments

This work was supported by the National Key R&D Program of China [2017YFC1405600]. ASAR and Radarsat-2 data were purchased from European Space Agency (ESA) and Canadian Space Agency (CSA).

References

Alpers, Werner (1985). Theory of radar imaging of internal waves. *Nature*, 314(6008): 245-247.

Claus, Alpers W, Hasselmann K (1990). Monte-Carlo simulation studies of the nonlinear imaging of a two dimensional surface wave field by a synthetic aperture radar. *Int. J. Remote Sens*, 11(10): 1695-1727.

Corcione V, Grieco G, Portabella M, et al. (2018). A Novel Azimuth Cutoff Implementation to Retrieve Sea Surface Wind Speed From SAR Imagery. *IEEE Trans. Geosci. Remote Sens*, 1-10.

Elfouhaily T , Chapron B , Katsaros K , et al (1997). A unified directional spectrum for long and short wind-driven waves. *J. Geophys. Res*, 102(C7): 15781.

Engen G, Johnsen H (1995). SAR-ocean wave inversion using image cross spectra. *IEEE Trans. Geosci. Remote Sens*, 33(4): 1047-1056.

Franceschetti G, Migliaccio M, Riccio D (1998). On ocean SAR raw signal simulation. *IEEE Trans. Geosci. Remote Sens*, 36(1): 84-100.

Ganguly D, Mishra M K, Chauhan P (2015). Deriving sea-state parameters using RISAT-1 SAR data. *Advances in Space Research*, 55(1): 83-89.

Grieco G , Lin W , Migliaccio M , et al (2016). Dependency of the Sentinel-1 azimuth wavelength cut-off on significant wave height and wind speed. *Int. J. Remote Sens*, 37(21): 5086-5104.

He Y. J (1999). Parametric method for extracting ocean wave direction spectrum by synthetic aperture radar. *Chinese Science Bulletin*, (04): 94-99. (in Chinese)

Hasselmann, Klaus, Hasselmann, Susanne (1991). On the nonlinear mapping of an ocean wave spectrum into a synthetic aperture radar image spectrum and its inversion. *J. Geophys. Res Oceans*, 96(C6): 10713.

Hasselmann S, C. Brüning, Hasselmann K, et al (1996). An improved algorithm for the retrieval of ocean wave spectra from synthetic aperture radar image spectra. *J. Geophys. Res*, 101.

He W, Jianhua Z, Jingsong Y (2012). A semiempirical algorithm for SAR wave height retrieval and its validation using Envisat ASAR wave mode data. *Acta Oceanologica Sinica*.

K. Hasselmann, R. K. Raney, W. J. Plant, et al (1985). Theory of synthetic aperture radar ocean imaging: A MARSEN view. *J. Geophys. Res*, 90(C3): 4659-4686.

Kerbaol V, Chapron B, Vachon P W (1998). Analysis of ERS-1/2 synthetic aperture radar wave

mode imagettes. *J. Geophys. Res*, 103(C4):7833.
Kerbaol V, Chapron B, Elfouhaily T, et al (1996). Fetch and wind dependence of SAR azimuth cutoff and higher order statistics in a mistral wind case. IEEE.
Kudryavtsev V, Akimov D, Johannessen J, et al (2005). On radar imaging of current features: 1. Model and comparison with observations. *J. Geophys. Res Oceans*, 110(C7).
Lyzenga D R (1986). Numerical Simulation of Synthetic Aperture Radar Image Spectra for Ocean Waves. *IEEE Trans. Geosci. Remote Sens*, 24(6): 863-872.
Li, H. M, Alexis, M, Wang H, et al (2019). Polarization Dependence of Azimuth Cutoff From Quad-Pol SAR Images. *IEEE Trans. Geosci. Remote Sens*.
Lin R, Yang J, Gang Z, et al. The significant wave height estimation by the azimuth cutoff of the quad-polarization SAR image[C]// Ocean Remote Sensing & Monitoring from Space. 2014.
Lyzenga D R , Malinas N P (1996). Azimuth falloff effects in two-antenna SAR measurements of ocean wave spectra. *IEEE Trans. Geosci. Remote Sens*, 34(4): 1020 - 1028.
Marghany M, Ibrahim Z, Genderen J V (2002). Azimuth cut-off model for significant wave height investigation along coastal water of Kuala Terengganu, Malaysia. *International Journal of Applied Earth Observation and Geoinformation*, 4(2): 0-160.
Mastenbroek C, De Valk C F (2000). A semiparametric algorithm to retrieve ocean wave spectra from synthetic aperture radar. *J. Geophys. Res*, 105(C2): 3497.
Phillips O M (1985). Spectral and statistical properties of the equilibrium range in wind-generated gravity waves. *Journal of Fluid Mechanics*, 156(-1): 505-531.
Stopa J E, Ardhuin F, Chapron B , et al (2015). Estimating wave orbital velocity through the azimuth cutoff from space‐borne satellites. *J. Geophys. Res Oceans*, 120(11).
J. Schulz-Stellenfleth, S. Lehner, D. Hoja (2005). A parametric scheme for the retrieval of two-dimensional ocean wave spectra from synthetic aperture radar look cross spectra. *J. Geophys. Res Oceans*, 110(C5).
Vachon P, Krogstad H, Scottpaterson J (1994). Airborne and spaceborne synthetic aperture radar observations of ocean waves. *Atmosphere*, 32(1): 83-112.
Ward K, Tough R, Watts S, et al (2013). Sea Clutter: Scattering, the K-Distribution and Radar Performance. 17(2): 233-234.
Wan, Y.; Zhang, X.; Dai, Y.; Shi, X (2019). Research on a Method for Simulating Multiview Ocean Wave Synchronization Data by Networked SAR Satellites. *J. Mar. Sci. Eng. 7*, 180.
Xu, X.J.; Li, X.F. Radar Phenomenological Models for Ships on Time-Evolving Sea Surface; *National Defense Industry Press*: Beijing, China, 2013; pp. 29-30. (in Chinese)
Yoshida T, Rheem C K (2013). SAR Image Simulation in the Time Domain for Moving Ocean Surfaces. *Sensors*, 13(4): 4450-4467.